RESEARCH ARTICLE

Key Points:
- Subtle ground deformation monitoring of Unimak Island
- Time series InSAR assisted by numerical weather prediction model
- Volcano source model study over Westdahl Volcano

Correspondence to:
W. Gong,
gwenyu@alaska.edu

Measurement and interpretation of subtle deformation signals at Unimak Island from 2003 to 2010 using weather model-assisted time series InSAR

**W. Gong[1], F. J. Meyer[1], C.-W. Lee[2], Z. Lu[3], and J. Freymueller[1]**

[1]Geophysical Institute, University of Alaska Fairbanks, Fairbanks, Alaska, USA, [2]National Institute of Meteorological Research, Korea Meteorological Administration, Seoul, South Korea, [3]Roy M. Huffington Department of Earth Sciences, Southern Methodist University, Dallas, Texas, USA

Abstract A 7 year time series of satellite radar images over Unimak Island, Alaska—site of Westdahl Volcano, Fisher Caldera, and Shishaldin Volcano—was processed using a model-free Persistent Scatterer Interferometry technique assisted by numerical weather prediction model. The deformation-only signals were optimally extracted from atmosphere-contaminated phase records. The reconstructed deformation time series maps are compared with campaign and continuous Global Positioning System (GPS) measurements as well as Small Baseline Subset interferometric synthetic aperture radar (InSAR) results for quality assessment and geophysical interpretation. We observed subtle surface inflation at Westdahl Volcano that can be fit by a Mogi source located at approximately 3.6 km north of Westdahl peak and at depth of about 6.9 km that is consistent with the GPS-estimated depth for the 1998 to 2001 time period. The magma chamber volume change decays during the period of 2003 to 2010. The deformation field over Fisher Caldera is steadily subsiding over time. Its best fit analytical model is a sill source that is about 7.9 km in length, 0.54 km in width, and located at about 5.5 km below sea level underneath the center of Fisher Caldera with strike angle of N52°E. Very little deformation was detected near Shishaldin peak; however, a region approximately 15 km east of Shishaldin, as well as an area at the Tugamak range at about 30 km northwest of Shishaldin, shows evidence for movement toward the satellite, with a temporal signature correlated with the 2004 Shishaldin eruption. The cause of these movements is unknown.

1. Introduction and Motivation

Many volcanic eruptions are preceded by pronounced ground deformation in response to increasing pressure from magma chambers or to the upward ascent of magma [*Dvorak and Dzurisin*, 1997] trigged by deep magma intrusion. This has been considered as one of the main precursory indicators before an eruption begins [*Dzurisin*, 2003]. Surface deformation measurements can be used to determine the location and shape of a volcanic pressure source beneath the surface [*Segall*, 2010]. Due to its independence from daylight and weather conditions, predictable repeat cycle, and high spatial resolution, synthetic aperture radar (SAR) interferometry (InSAR) distinguishes itself as a tool for a long-term deformation monitoring over volcanoes. InSAR measures the uplift or subsidence associated with eruptions or magma intrusions as a phase change between repeated acquisitions captured in interferograms. It is especially useful for the monitoring of remote regions, for which maintaining in situ geodetic measurements remains difficult.

In this paper, we document the temporal evolution of deformation patterns for the period of 2003 to 2010 over Unimak Island, the largest island of Alaska's Aleutian Island chain [*Wood and Kienle*, 1990] (Figure 1). It is home to several volcanoes including Roundtop, Isanotski, Shishaldin, Fisher, Westdahl, and Pogromni from east to west. Three of these volcanoes (Shishaldin, Fisher, and Westdahl) have experienced historical activity, for instance, the latest eruption of Shishaldin was in 2014 and Westdahl last erupted in 1991 [*Alaska Volcano Observatory*, *A*, 2009]. Fisher has been less active than its neighbors since the twentieth century; however, previous studies observed continuous subsidence around the center of Fisher Caldera. Based on a short record of GPS measurements (1998 to 2001), *Mann and Freymueller* [2003] have hypothesized that the cause of subsidence is depressurization of hydrothermal system or thermal contraction and degassing of a crystallizing dike. Unimak Island is also seismically active. There were more than 800 volcanic-tectonic
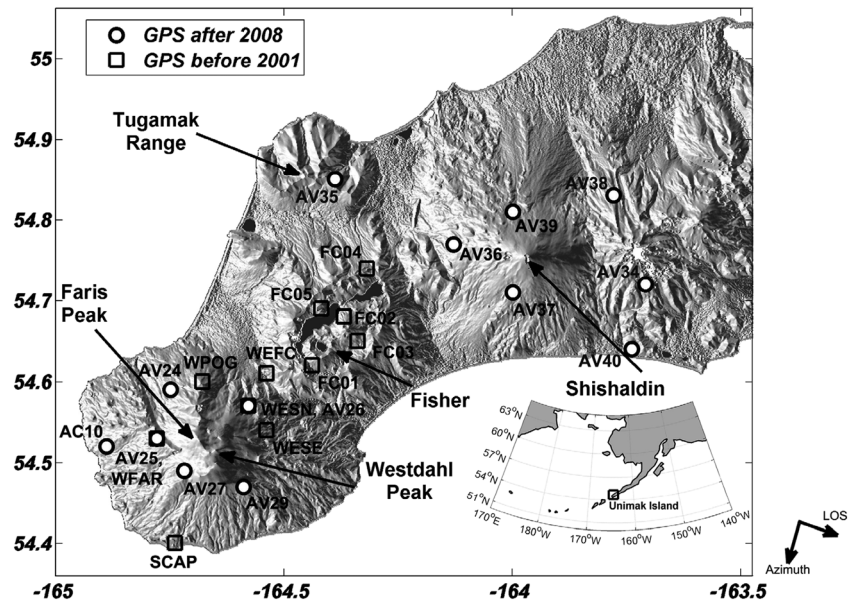
Figure 1. The location of the three studied volcanoes, Westdahl, Fisher, and Shishaldin, and GPS sites on Unimak Island with shade relief topographic maps background. The satellite line-of-sight (LOS) direction and flight direction (azimuth) are denoted on the lower corner. The campaign GPS sites between 1998 and 2001 [*Mann and Freymueller*, 2003] are denoted by black squares; they are SCAP, WFAR, WESE, WESN, WPOG, WEFC, FC01, FC03, FC02, FC05, and FC04 from south to north. Continuous GPS after 2008 are denoted by black circles with white filling; they are AC10, AV25, AV24, AV27, AV29, AV26, AV35, AV36, AV39, AV37, AV38, AV40, and AV34 from the west to the east.

earthquakes recorded during the period of 2003 to 2010 over Westdahl and Shishaldin, according to the *Alaska Volcano Observatory*, *A* [2009] earthquake catalogue.

The remoteness of Unimak Island has limited its geophysical studies; e.g., there were no GPS measurements around the active volcanoes on Unimak Island during 2001 to 2008 and seismic equipment failure led to a seismic data outage during the period of 2006 to 2008 [*Buurman*, 2013]. We used radar interferometric satellite remote sensing techniques to retrieve the surface deformation history of Unimak Island for the period of 2003 to 2010.

The value and applicability of InSAR for geodynamic monitoring applications is limited by temporal decorrelation, especially for nonurban areas, due to unstable and complex ground coverage, as well as electromagnetic path delay variations when the radar signal propagates through the atmosphere (ionosphere and troposphere), reducing both the sensitivity and accuracy of the technique [*Hanssen*, 2001]. Particularly, problematic artifacts in radar images (e.g., C-band and X-band) are caused by temporal variations in weather conditions that can be significant on tall volcanic edifices. Also, snow coverage often limits the amount of useful coherent data in subarctic environments [*Lu and Freymueller*, 1998]. Thus, in the present study, an advanced InSAR technique, namely, a weather model-supported Persistent Scatterer InSAR (PSI) approach, is used for deformation history reconstruction from C-band InSAR time series. Both atmospheric artifacts and other nondeformation phase artifacts are treated through a PSI processing technique that combines information provided by numerical weather prediction (NWP) models with the deformation model-free PSI technique [*Hooper et al.*, 2012]. The choice of using NWP products is due to the fact that frequent cloud coverage over the Aleutians limits the usefulness of multispectral satellite sensor water vapor products. The atmospheric delays simulated by regional NWP forecasts are not directly subtracted from interferograms to reconstruct the subtle deformation in this study. It is because of their limited quality in reproducing the spatial pattern of atmospheric delays [*Foster et al.*, 2013; *Gong et al.*, 2013; *Cimini et al.*, 2012; *Liu*, 2012]. Instead, NWP-derived atmospheric statistics are integrated into the PSI processing to optimize a filter for removing the atmospheric delays. To further support our result, we also applied small baseline time series InSAR methods to the same SAR data set for comparison.

The extracted deformation result is confirmed with the comparison to GPS measurements within the limited temporal overlap period from 2008 to 2010. Afterward, the PSI-extracted deformation time series are used for the volcano source model inversion at Westdahl Volcano and Fisher Caldera, and for the geophysical interpretation of activity at Shishaldin Volcano.

2. Unimak Island and Its Previous Geodetic Studies

Surface deformation on Westdahl Volcano was studied in previous efforts both from radar satellite remote sensing and GPS studies. Standard differential InSAR techniques have been applied to study posteruption inflation from 1993 to 1998 [*Lu et al.*, 2003, 2000], 1991 to 2000 [*Lu et al.*, 2003], and 2003 to 2010 [*Lu and Dzurisin*, 2014] after its eruption in 1991. These studies suggest that Westdahl Volcano was inflating in an exponentially decaying fashion. *Mann and Freymueller* [2003] used GPS measurements acquired from 1998 to 2001 to analyze Westdahl's surface deformation and characterized its magma chamber properties. The GPS-determined volcanic source depth of Westdahl [*Mann and Freymueller*, 2003] is deeper than that of the InSAR result; nevertheless, it also suggested that the volume change was slowing down over time. There is a slight inconsistency in the horizontal location of the source, with the GPS study finding a location somewhat north of the InSAR study. However, both studies suggested that a point source model [*Mogi*, 1958] was sufficient for modeling the deformation at Westdahl Volcano.

Fisher Caldera, which contains several active fumaroles and two large lakes, is one of the largest calderas in the Aleutian Islands [*Lu et al.*, 2007] and is located east of Westdahl. The southern part of Fisher is covered by a thick layer of tephra, which offers the potential for achieving excellent coherence in InSAR studies. Previous work showed subsidence of up to 3 cm during the period of 1993 to 1995 [*Lu et al.*, 2007] measured with InSAR and 1998 to 2001 from GPS measurements [*Mann and Freymueller*, 2003] (square markers in Figure 1), which may be due to the degassing and thermal contraction of a crystallizing subsurface magma body and/or depressurization of the corresponding hydrothermal system.

In the center of Unimak Island, Shishaldin Volcano, a stratovolcano that is the highest peak of the island, has more than 20 recorded eruptions during recorded history. Several of these eruptions have occurred since the 1990s, including four explosive eruptions in 1995, 1997, 1999, and 2004 and an effusive eruption in 2014 [*Alaska Volcano Observatory*, A, 2009]. However, previous satellite InSAR studies observed no significant deformation in the coherent region surrounding the volcano for the eruptions in the 1990s, which suggests a deep volcanic reservoir (more than 10 km) or a rapid magma refilling that compensated for the preeruption inflation and/or a very shallow depth for the magma chamber [*Lu*, 2007; *Lu et al.*, 2007; *Moran et al.*, 2006].

3. Technique Background and InSAR Data Processing

In this study, special attention has been paid to separate the deformation field from nondeformation artifacts in the InSAR observations. Strong atmospheric artifacts have been observed in this region that can mimic volcano inflation [*Lu et al.*, 2003; *Lu and Dzurisin*, 2014].

We use PSI techniques to mitigate the problem of ground decorrelation that is often observed for natural terrains over long time intervals. We apply a deformation model-free PSI method due to its higher performance for applications in geophysically active regions [*Hooper et al.*, 2012]. The processing parameter optimizations in PSI data processing, especially the optimal temporal filter determination, need to be carefully carried out to ensure that the most accurate results are generated and subtle deformation signals are preserved, especially with temporal gaps in data set [*Gong and Meyer*, 2012]. Thus, an advanced InSAR approach is used in this study, where PSI processing is assisted by statistical atmospheric delay information that is extracted from NWP data.

In this study, 23 scenes of Environmental Satellite advanced synthetic aperture radar (ASAR) data acquired in descending mode during the period of July 2003 to August 2010 are used for deformation history reconstruction. Specifically, only the snow-free season scenes, mainly acquired from May to October, are used due to their favorable seasonal ground coverage condition that improves the interferometric coherence. The image acquired on 22 September 2006 was discarded from the PSI processing due to its large spatial baseline.

Table 1. Parameters of Single-Master Interferograms

No.	Date	$B_\perp$ (m)	B_t (day)	f_{DC} (Hz)	var_{aps} (rad^2)
1	20 June 2003	−660	−1540	294	0.58
2	25 July 2003	−775	−1505	254	0.09
3	29 August 2003	−258	−1470	218	0.62
4	4 June 2004	−69	−1190	179	0.32
5	9 July 2004	−521	−1155	185	0.30
6	13 August 2004	−626	−1120	167	10.57
7	17 September 2004	427	−1085	187	0.26
8	22 October 2004	−94	−1050	235	1.29
9	24 June 2005	106	−805	160	0.29
10	29 July 2005	−56	−770	211	0.21
11	2 September 2005	405	−735	211	1.14
12	7 October 2005	−687	−700	258	4.00
13	9 June 2006	−674	−455	207	0.52
14	14 July 2006	342	−420	224	0.14
15	7 September 2007(master)	0	0	0	0
16	18 July 2008	−261	315	229	0.24
17	22 August 2008	−58	350	223	0.46
18	26 September 2008	−728	385	205	0.23
19	7 August 2009	−404	700	222	0.58
20	11 September 2009	186	735	219	0.13
21	23 July 2010	−721	1050	229	0.82
22	27 August 2010	−373	1085	228	0.54

3.1. Time Series InSAR Processing Assisted by Numerical Weather Prediction Model
3.1.1. Phase Components Decomposition and InSAR Data Processing

The unwrapped differential interferometric phase components at pixel p in interferogram i can be written as equation (1) [*Ferretti et al.*, 2000; *Hooper et al.*, 2012].

$$\phi_{p,i} = \phi_{p,i,\text{topo}} + \phi_{p,i,\text{defo}} + \phi_{p,i,\text{orbit}} + \phi_{p,i,\text{atm}} + \phi_{p,i,\text{noise}} \tag{1}$$

where $\phi_{p,i,\text{topo}}$ is the residual topographic phase component due to the inaccuracy of the topography model used in the differential interferogram formation, $\phi_{p,i,\text{defo}}$ is the contribution of ground deformation, $\phi_{p,i,\text{orbit}}$ denotes the residual phase due to errors in the satellite orbits, $\phi_{p,i,\text{atm}}$ is the atmospheric distortion that consists of a slave component $\phi_{p,i,s-\text{atm}}$ and a master component $\phi_{p,i,m-\text{atm}}$, and the last term $\phi_{p,i,\text{noise}}$ is the phase noise component (e.g., system thermal noise and decorrelation noise) that is presumed to be relatively small for a phase-stable pixel in PSI studies.

Twenty-one single-master interferograms were formed and processed for deformation monitoring, and 89,778 phase-stable pixels were found, and their phase components $\phi_{p,i,\text{topo}}$ and $\phi_{p,i,m-\text{atm}}$ were removed through a standard model-free PSI processing [*Hooper et al.*, 2012]. The corresponding image acquisition times, baseline information, and spatial variances of differential atmospheric delays computed from NWP products (var_{aps}) are listed in Table 1. The data set shows strong atmospheric distortions (e.g., 13 August 2004 and 17 October 2005) and large time gaps ranging from 245 to 420 days over winter resulting in a small data stack over a large time span with severe atmospheric artifacts.

As the main purpose of this study is for volcanic deformation monitoring, $\phi_{p,i,\text{orbit}}$ is modeled by a planar ramp and subtracted from $\phi_{p,i}$. After removing those components (referred to as preprocessing in this paper), the remaining phase signal ($\tilde{\phi}_{p,i}$) contains $\phi_{p,i,s-\text{atm}}$, $\phi_{p,i,\text{defo}}$, and a nuisance term $\varepsilon_{p,i}$ as shown in equation (2). $\varepsilon_{p,i}$ contains $\phi_{p,i,\text{noise}}$ and residuals of the largely eliminated signals of $\phi_{p,i,\text{topo}}$, $\phi_{p,i,m-\text{atm}}$, and $\phi_{p,i,\text{orbit}}$.

$$\tilde{\phi}_{p,i} = \phi_{p,i,\text{defo}} + \phi_{p,i,s-\text{atm}} + \varepsilon_{p,i} \tag{2}$$

After preprocessing, the conventional procedure separates $\phi_{p,i,\text{defo}}$ from $\tilde{\phi}_{p,i}$ (equation (2)) through a spatial-temporal low-pass filter based on the expectation that atmospheric signals are temporally decorrelated and spatially correlated over a small scale, while deformation signals are correlated both in time and space [*Hooper et al.*, 2012]. Thus, $\phi_{p,i,s-\text{atm}}$ is mitigated via a low-pass filter in the temporal

domain. The mathematical representation of this filter is written in equation (3), in which t is the temporal baseline for each interferogram and $g(t, T)$ is a low-pass filter realized by the weighted temporal smoothing with length T. The low-pass signal $\left(\widetilde{\phi}_{p,i}\right)_{\mathrm{lp}}$ is the estimate of the deformation component.

$$\left(\widetilde{\phi}_{p,i}(t)\right)_{\mathrm{lp}} = \sum_{\tau=0}^{t} \widetilde{\phi}_{p,i}(\tau) \cdot g(t - \tau, T) \tag{3}$$

Notice that in order to preserve deformation signals and reduce atmospheric artifacts, either knowledge of deformation field or of the atmospheric delays is needed to properly construct $g(t, T)$, e.g., using auxiliary geodetic data sets to identify the adequate smoothing weight [*Schmidt and Burgmann*, 2003]. In many cases, including the present study, the temporal evaluation of the deformation during the studied time span is not known, so in our method, $\phi_{p,i,\mathrm{defo}}$ is extracted from equation (2) by applying an atmospheric filter optimization with the assistance of statistics extracted from NWP-produced atmospheric delay maps.

3.1.2. Advanced Atmospheric Signal Mitigation

#### 3.1.2.1. General Theory and Algorithm Realization

Although NWP forecast products, the only feasible atmospheric auxiliary data source in this study, have limited accuracy to reproduce the atmospheric delay spatial pattern, they have been tested to be able to provide the atmospheric delay statistics [*Gong et al.*, 2011]. It has established a robust linear correlation between atmospheric delay spatial variance from NWP forecast $\sigma_{i,\mathrm{nwp}}^2$ as a prior and $\sigma_{i,\mathrm{ifg}}^2$ captured in interferogram time series. This linear relation is controlled by a single-scale factor, whose value is not fixed but is related to the parameterization of the NWP runs. In other words, NWP simulations are capable of reproducing the temporal changes of $\sigma_{i,\mathrm{ifg}}^2$. Such stochastic atmospheric delay information can be used to guide the correction of atmospheric delay artifacts in time series InSAR data processing.

Thus, the main concept of our temporal filter optimization is to use the prior $(\sigma_{i,\mathrm{nwp}}^2)$ that are computed from the explicit data source, e.g., NWP-simulated atmospheric delays at every SAR image acquisition time, to constrain the definition of $g(t, T)$ for atmospheric signal mitigation. Assuming that (a) the low-pass filter $g(t, T)$ could be formed properly and (b) the nuisance term $\varepsilon_{p,i}$ has been minimized, e.g., with carefully conducted data preprocessing, the high-pass signals $\left(\widetilde{\phi}_{p,i}\right)_{\mathrm{hp}}$ that are computed from $\left(\widetilde{\phi}_{p,i}\right)_{\mathrm{hp}} = \widetilde{\phi}_{p,i} - \left(\widetilde{\phi}_{p,i}\right)_{\mathrm{lp}}$ are a good estimate of the $\phi_{p,i,s-\mathrm{atm}}$ time series. Hence, the spatial variance $(\sigma_{i,\mathrm{hp}}^2)$ of $\left(\widetilde{\phi}_{p,i}\right)_{\mathrm{hp}}$ is an adequate estimate of $\sigma_{i,\mathrm{ifg}}^2$ so that the linear relationship between $\sigma_{i,\mathrm{nwp}}^2$ and $\sigma_{i,\mathrm{hp}}^2$ exists. Consequently, even without any knowledge on the deformation field, the optimal low-pass filter length $\hat{T}$ can be chosen by maximizing the linear correlation between $\sigma_{i,\mathrm{nwp}}^2$ and $\sigma_{i,\mathrm{hp}}^2$.

The algorithm to define the optimal $\hat{T}$ is implemented with a grid search-based approach. The lower bound is defined as the satellite revisit period to guarantee at least three samples in the filter window, if not considering the temporal gap. The upper bound is used to aid the efficiency of computation, e.g., 350 days used in this experiment. That is, for every $\hat{T}$ candidate, the corresponding $\sigma_{i,\mathrm{hp}}^2$ series is computed and compared to the prior $\sigma_{i,\mathrm{nwp}}^2$ and the $\hat{T}$ that maximizes the linear correlation, which can be evaluated by coefficient of determination or equivalent statistics, is considered to be the optimal filter parameter. The Gaussian-shaped kernel for $g(t, T)$ is suggested, given it weights the closer acquisition over distant ones and its simple parameterization. The standard deviation of the Gaussian kernel is defined as its window size ($\hat{T}$) and needed to be optimized. Based on various applications and research purposes, the other filter kernels could also been used and the searching algorithm can be adjusted. Due to the unknown properties of the spatial-temporal covariance of either deformation or atmosphere signal, the temporal filter is applied globally, which would be suitable for the smooth deformation signal reconstruction.

3.1.2.2. Data Processing in the Study of Unimak Island

In this study, the Weather Research and Forecast (WRF) model [*Skamarock et al.*, 2008] (version 3.5) was used to simulate the atmosphere in three dimensions (3-D). Initial boundary conditions from National Centers for Environmental Prediction Final data [*University Corporation for Atmospheric Research*, 2013] were used as input for the WRF runs. We used an approximately 9 h forecasting period and 1 km horizontal resolution setup for model outputs. The refractivity index was computed at each resolution grid cell and integrated in
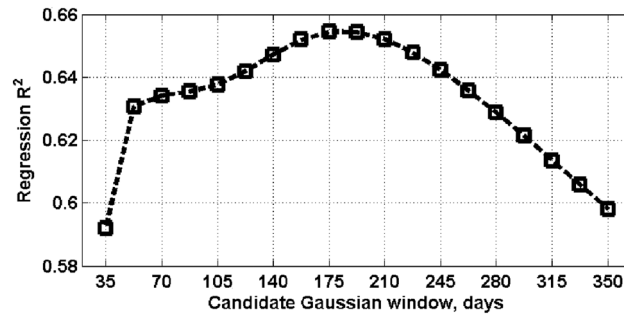
Figure 2. Demonstration of the optimal window determination; *x* axis is the candidate window search space; *y* axis is the coefficient of determination (R^2) computed from the regression of $\sigma_{i,\mathrm{nwp}}^2$ and $\sigma_{i,\mathrm{hp}}^2$ data pairs.

the satellite line-of-sight (LOS) direction to produce integrated absolute atmospheric delay maps. Afterward, the simulated atmospheric phase screens (APSs) were computed through differential delay maps corresponding to the SAR image acquisition times, and the temporal mean was subtracted from every simulated APS to approximate the master atmospheric component reduction; a linear planar trend also is removed from the simulated APSs. In the end, the NWP-simulated APSs were resampled to 300 m resolution grid in radar coordinates and then were used to compute the $\sigma_{i,\mathrm{nwp}}^2$ that assists the extraction of $\phi_{p,i,\mathrm{defo}}$ from $\widetilde{\phi}_{p,i}$.
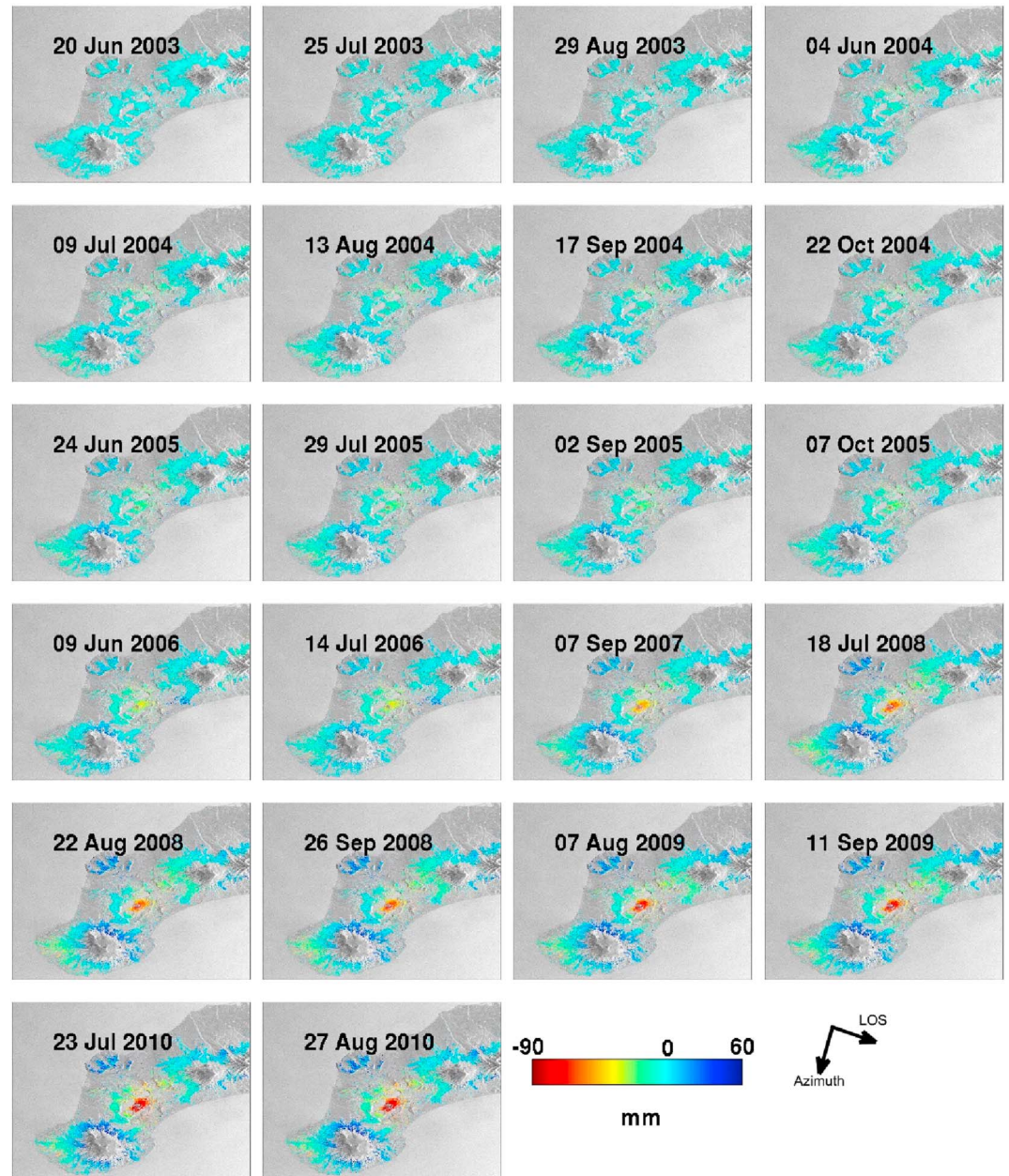
We have carefully conducted the 3-D phase unwrapping at persistent scatterer (PS) points and preprocessing steps to remove topography residuals and orbit errors. The preprocessed PSI phases were resampled to the same resolution as the NWP-produced APSs that would also further reduce spatial uncorrelated noises. Thus, the nuisance term $\varepsilon_{p,i}$ in equation (2) has been minimized. Afterward, we implemented the searching algorithm on the resampled PSI phases to determine the optimal window length $\hat{T}$ of the Gaussian kernel. The search space of $\hat{T}$ was bounded within the range from 35 days to 350 days and gridded by the half of the satellite revisiting time (17.5 days). Window length $\hat{T}$, which maximizes the coefficient of determination (R^2) in the linear regression through origin with $\sigma_{i,\mathrm{hp}}^2$ and the known $\sigma_{i,\mathrm{nwp}}^2$ series, has been selected as the optimal filter length. The selection step can be visualized in Figure 2, which demonstrates the corresponding R^2 value versus the candidate space of $\hat{T}$. It shows that at window size setting of 175 days, the corresponding $\sigma_{i,\mathrm{hp}}^2$ fits the best to the linear model with the prior $\sigma_{i,\mathrm{nwp}}^2$.

Afterward, back to the standard model-free PSI processing, we have applied the low-pass filter with the optimal setting $\hat{T}$ of 175 days to the original preprocessed single-look phases $\widetilde{\phi}_{p,i}$. Then, we can finalize the reconstruction of the deformation time series of Unimak Island in LOS direction (toward the satellite is positive) as demonstrated in Figure 3, which shows subtle but continuous deformation across Unimak. Also shown in Figure 3, the detected PS points locate in lower level to medium-level elevation, which is because the snow and ice cover at high altitude (e.g., the tops of Shishaldin Volcano and Westdahl Volcano) and vegetation at lower altitude.

3.2. Small Baseline Time Series InSAR

Within the study time span there are few other geodetic observations for testing against; thus, we cross processed our data using a Small Baseline Subset (SBAS) InSAR technique to check our PSI-based results. Hence, the SBAS result is used as a reference only, and a comparison of the techniques for the deformation detection and long-term monitoring was considered beyond our scope. A technique comparison can be found in previous literature [*Agram et al.*, 2011]. In our implementation, the SBAS method first divides the unwrapped interferograms into two stacks, including low-quality and high-quality subsets. The latter are used for correcting potential phase unwrapping errors in the low-quality interferograms, and then both are used together for displacement estimation. Unlike the single-master PSI approach, the SBAS method uses interferograms with short temporal and perpendicular baselines in order to minimize the nondeformation signals and maximize the coherence. The targeted scatterers in SBAS approaches are the distributed scatterers, while PSI methods focus on the so-called persistent scatterers (PSs), which are supposed to be more stable in the natural environment for long time span studies [*Hooper et al.*, 2012]. The implementation steps of SBAS include the selection and formation of small baseline interferograms, phase unwrapping, phase inversion through singular value decomposition, and mitigation of nondeformation signals (for detail please refer to *Lee et al.* [2010]). From the original 22 SAR images (see Table 1), 42 small baseline interferograms were generated and 21 of them were selected to form the high-quality interferogram subset. In the end, the

Figure 3. Deformation time series reconstructed by PSI data processing. The studied time span is from 2003 to 2010 that covers the eruption of Shishaldin Volcano in February to May 2004.

displacements at the 21 SAR acquisition times were processed and recovered, because the image acquired on 9 July 2004 was discarded in the SBAS processing due to its unfavorable coherence conditions. In Figure 4, the average linear deformation velocity derived from both PSI and SBAS approaches are plotted side by side for visual comparison. Note that the true deformation rate may not be linear with time.

Both methods have detected common deformation features, including a subtle movement toward the satellite around Westdahl and a stronger movement away from the satellite at Fisher Caldera. The value of computed correlation coefficient of deformation linear rate maps derived separately by PSI and SBAS is 0.82. For every PS target, we also computed the ratio of linear rate difference between PSI ($v_{PSI,p}$) and SBAS ($v_{SBAS,p}$) approaches (as $|(v_{PSI,p} - v_{SBAS,p})/v_{SBAS,p}|$) to quantitatively demonstrate the inconsistency between the SBAS- and PSI-derived velocities. The median value of this ratio is about 7%, and 89% of the total PS pixels has the ratio value smaller
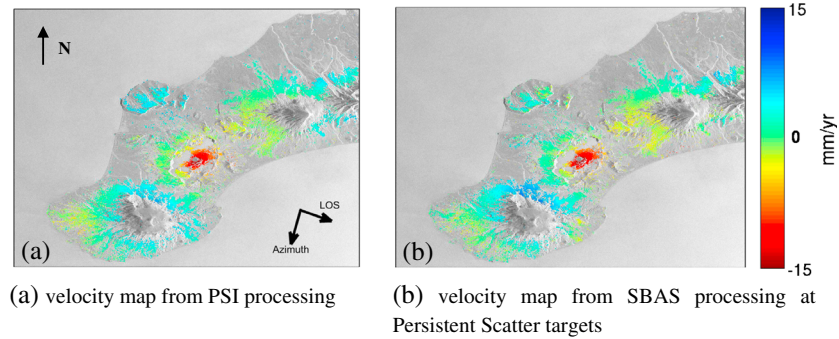
(a) velocity map from PSI processing (b) velocity map from SBAS processing at Persistent Scatter targets

Figure 4. Velocity maps from (a) PSI and (b) SBAS processing, respectively.

than20%. Overall, the PSI-derived average velocity map shows similar quality to the one from SBAS method at the majority of selected PS targets. Figure 5 shows an example of a pointwise comparison for Fisher Caldera, where the extracted about maximum subsidence captured by the PSI and SBAS methods are compared. A coherent target in the SBAS map was selected in the center region of Fisher Caldera. An area of approximately 200 m radius was searched for corresponding PSI points, and five targets were found within the search space. The averaged time series of the SBAS (gray dashed line with square marker) and PSI points (black dashed line with circle marker) are relative to the image acquired on 7 September 2007 and are spatially referenced to the spatial average of overall displacement computed from each measurement separately. In this example, the time series from PSI and SBAS are significantly correlated with each other through the statistic test and the ratio of linear rate difference is about 20%.

4. Geophysical Study Based on InSAR Result

Based on the deformation maps in Figure 4, we can identify subtle movements toward the satellite around Westdahl and observe subsidence signals over Fisher Caldera. Moreover, it is notable that Tugamak range as well as the east side of Shishaldin shows subtle deformation (Figure 4) while the rest of the island shows essentially no ground deformation. In this section, the PSI results are further compared to historical and current GPS measurements and are used jointly for geophysical interpretation. Focusing on Westdahl Volcano and Fisher Caldera, volcanic source model inversions are applied and presented in section 5.

4.1. Comparison With In Situ Geodetic Measurement

There are two sets of GPS measurements available over Unimak, including the campaign GPS data covering the time of 1998 to 2001 [*Mann and Freymueller*, 2003] and current Plate Boundary Observatory (PBO) continuous GPS measurements covering the time from 2008 [*University NAVSTAR Consortium* (*UNAVCO*), 2013]. The two data sets involve different sites with no overlap, and there were no measurements between 2001 and 2008. It is possible that the rate of deformation was different during the two time periods. The PSI results are compared to GPS time series and velocities to better understand the overall deformation history.

Figure 5. An example of LOS displacements (millimeter) at the center of Fisher Caldera in 2003 to 2010 from SBAS and PSI processing.

4.1.1. Comparison With GPS Measurements Before 2001

There were seven GPS campaign sites around Westdahl and five around Fisher Caldera during the period from 1998 to 2001 (Figure 1) [*Mann and Freymueller*, 2003]. The GPS positions were computed in the International Terrestrial Reference Frame 1997, and velocities were referenced to the site KATY at the east end of the island [*Freymueller and Beavan*, 1999]. The details of the comparison between the GPS- and PSI- measured LOS deformation velocities
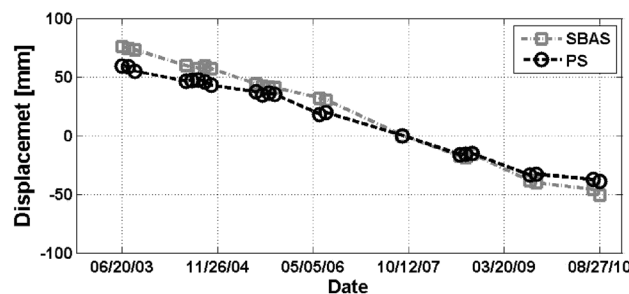
Table 2. GPS Velocity (mm/yr) in LOS Direction During 1998–2001 and PSI Velocity During 2003–2010

Site	Latitude	Longitude	GPS V-LOS[a]	PSI V-LOS[b]	PSI V-LOS Corrected	No. PSI	Mean Distance (m)
SCAP	54.4	−164.74	5.3 ± 4.7	1.2 ± 0.5	1.3 ± 0.5	3	131
WESE	54.54	−164.54	5.0 ± 5.6	4.8 ± 0.1	4.9 ± 0.1	3	246
WESN	54.57	−164.58	19.9 ± 5.6	5.4 ± 0.5	5.4 ± 0.5	4	216
WPOG	54.6	−164.68	2.2 ± 3.7	1.3 ± 0.2	1.4 ± 0.2	2	430
WFAR	54.53	−164.78	1.3 ± 3.7	-0.3 ± 0.6	-0.2 ± 0.6	2	99
WEFC	54.61	−164.54	10.3 ± 3.8	2.5 ± 0.5	2.6 ± 0.5	2	235
FC01	54.62	−164.44	-3.8 ± 5.6	-1.9 ± 0.6	-1.8 ± 0.6	3	219
FC02	54.68	−164.37	-11.6 ± 3.8	-11.7 ± 0.6	-11.6 ± 0.6	4	33
FC03	54.65	−164.34	-11.1 ± 2.8	-10.7 ± 0.7	-10.6 ± 0.7	5	138
FC04	54.74	−164.32	-2.8 ± 3.8	-3.6 ± 0.4	-3.5 ± 0.4	4	236
FC05	54.69	−164.42	6.6 ± 4.7	-2.9 ± 0.03	-2.8 ± 0.03	2	74

[a]GPS LOS uncertainty is computed from its 3-D uncertainties in 1 sigma.
[b]PSI uncertainty is the standard deviation of the velocities at selected points.

are shown in Table 2, together with the GPS sites' location, the number of selected PSI points nearby, and the average distance from the PSI points to each GPS station. The distance thresholds are determined adaptively with 50 m per step to guarantee that at least two PSI points are chosen. The PSI results from 2003 to 2010 are adjusted so that the mean LOS displacement over each image is zero (Table 2). Note that the SAR image has no sensitivity to the ground deformation parallel to the satellite track (azimuth direction) because it records only the deformation in the LOS direction, perpendicular to the satellite track (shown in Figure 1). Hence, the 3-D GPS velocities and uncertainties (see Table 2) given by *Mann and Freymueller* [2003] were projected into the SAR LOS direction for comparison with PSI measurements.

The uncertainties of the PSI results are the standard deviation of the velocities at the PSI points within the given distances. Two GPS sites (WESS and PANK) are not included in Table 2 because there were not sufficient PSI points nearby or because the site was outside of the image spatial coverage. GPS sites named with the prefix "WE" as well as site SCAP surround Westdahl peak, and the prefix "FC" denotes the sites around Fisher Caldera.

First of all, the bias introduced by the different reference frames of the PSI and GPS velocities needs to be removed. However, due to the fact that the majority of PSI points is close to active volcanoes and there is no SAR image coverage over the GPS reference point KATY at the east end of the island, we applied an alternative method to determine the reference difference between the GPS and PSI velocities. We computed the difference between the velocities of GPS site FC02 and its surrounding PSI points and assume that this difference is only from the spatial reference difference. This method is implemented based on the following considerations: (a) the GPS result for FC02 has high quality and the smallest average distance to the surrounding PSI points; (b) this area has a high PSI point density and a high deformation-to-noise ratio; and (c) as suggested in previous studies [*Mann and Freymueller*, 2003], Fisher Caldera is subsiding linearly (Figure 5). Thus, if there is any difference caused by the reference frame difference between PSI and GPS results, it should be linear in time. Therefore, the velocity offset of about 0.1 mm/yr (PSI minus GPS) caused by the reference frame difference was subtracted from the corrected PSI velocities listed in the sixth column of Table 2. Such a small correction is not a surprise, because the GPS study suggested that most of the island did not move relative to KATY [*Mann and Freymueller*, 2003].

Comparing the corrected PSI velocities after 2003 and GPS measurements from 1998 to 2001 (Table 2, sixth column), the inflation rate of Westdahl Volcano has decreased with time. Most of the region around Westdahl is still moving toward the satellite (the LOS direction) but with a velocity less than 1 cm/yr. The subsidence rate of Fisher Caldera is very consistent between the GPS and InSAR observations. Around Fisher Caldera, the difference between the PSI velocities and the GPS measurement is less than 2 mm/yr except for FC05. This difference is well within the error bound of the GPS results.

4.1.2. Comparison With GPS Measurements After 2008

Since 2008, the PBO includes a continuous GPS network [*UNAVCO*, 2013] on Unimak Island that mainly covers Westdahl and Shishaldin volcanoes. There are 13 sites available with 3 years (2008–2010) of overlap with the PSI study time period as shown in Figure 1. Site AV40 has been excluded from this comparison due to

Table 3. Statistical Analysis of the Displacement Residuals From PBO Continuous GPS and PSI in the Overlap Dates, Residuals Computed From GPS Minus PSI[a]

| Site Name	Latitude	Longitude	Height (m)	Points No.	Mean Distance (m)	Residual Offset (mm)		Residual σ (mm)	
						Opt. Win.	70 days	Opt. Win.	70 days
AC10	54.52	−164.89	170.45	3	115.61	0.77	0.76	2.74	2.78
AV24	54.59	−164.75	481.72	4	60.77	0.08	0.28	4.78	4.98
AV25	54.53	−164.78	651.94	3	78.19	6.00	5.87	6.55	6.43
AV26	54.57	−164.58	577.59	2	103.23	11.46	11.67	12.26	12.44
AV27	54.49	−164.72	977.91	3	413.48	0.67	0.13	3.01	3.46
AV29	54.47	−164.59	971.88	2	887.67	0.88	0.59	5.40	5.40
AV34	54.72	−163.71	636.38	2	366.69	0.41	−0.27	8.95	11.56
AV35	54.85	−164.39	646.98	4	357.12	4.30	4.32	6.12	6.36
AV36	54.77	−164.13	648.40	3	36.02	0.20	−0.04	7.70	7.84
AV37	54.71	−164.00	796.03	3	312.40	3.64	3.84	5.06	5.97
AV38	54.83	−163.78	492.29	3	29.58	2.74	2.23	5.14	4.91
AV39	54.81	−164.00	797.38	2	522.42	−0.71	−1.93	5.16	6.28

[a]Locations of GPS sites can be found in Figure 1. From left to right, they are site name, latitude, longitude, and height location of GPS sites, number of selected PS points, the average distance between PS points and GPS station, the mean value (offset) of residuals, and the standard deviation (σ) of residuals.

large residuals in the PSI processing near this point, which are likely related to the low PS point density in this area. The geographic information of the remaining 12 sites is listed in Table 3. Here we compare the time series computed from PSI and GPS as shown in Figure 7 for Westdahl sites and Figure 8 for Shishaldin sites. The only eruption event that occurred on Unimak Island within the studied time span, Shishaldin eruption in February to May 2004, is also marked by vertical dashed lines. The number of PSI points near each GPS site is listed in Table 3, including their average distance from the GPS site.

Shown in Figures 7 and 8, a 10 day moving average has been applied to every GPS daily measurements to reduce both the noise and effects from the short-term deformation that could not be captured by the ASAR mission (35 days revisiting period). Both the time-averaged GPS measurements and corresponding error bounds (blue markers) at SAR acquisition dates are highlighted for a better visualization of the comparison to PSI results (red markers). The GPS error bounds in the LOS direction are computed from the uncertainties of the GPS 3-D positions, and the PSI error bound is the standard deviation of the PSI points surrounding the GPS instrument locations. Due to impacts of snow accumulation on the GPS antennas (J. Freymueller, GPS position bias from the accumulation of snow on the GPS antenna personal Communication, 2014), GPS records during the winter period (December to the following May) for AV27, AV29, AV35, AV37, and AV39 were removed from figures and analysis. Given that all the SAR acquisitions are during the local Alaska summer period, this only affects sites by reducing a few weeks of GPS data from the overlapping sample set.

The time series are referenced to the earliest date of the temporal overlap between the PSI and GPS. The PSI time series are referenced so that the spatial average displacement in every interferogram frame is zero, while the PBO GPS measurements are relative to a North America fixed reference frame based on ITRF2008 (NAM08). To put the PSI and GPS in the same reference frame, the linear rates of the GPS and PSI from 2008 to 2010 are computed separately from their measurements within the common time interval. The rate differences (GPS rate minus PSI) are shown in Figure 6 by square markers and the posterior error bound is denoted by black vertical bars. The remaining 12 sites are used to compute the weighted average velocity shift between the GPS and PSI (0.98 mm/yr), which is visualized and denoted by the dashed gray line in Figure 6. This average rate difference is taken as the spatial reference frame difference between the GPS and PSI and is removed from PSI displacement time series. The PSI results given in Figures 7 and 8 and Table 3 are measurements after the spatial reference compensation. This reference frame difference determination method is applied due to the difficulty in defining a proper reference area in the PSI measurements given that most PSI points are near active volcanoes and is based on the following assumptions: (1) the reference frame difference is assumed to be linear in time and (2) all linear rate differences between the GPS and PSI are due to the different reference frame or random noise.

In Figure 7, the PSI and GPS measurements are plotted together for interpretation. The time series are given as one-way displacements. Around Westdahl Volcano, station AC10 hardly shows any linear trend during the overall time span (Figure 7). The AC10 PSI time series indicates a slight movement away from the satellite
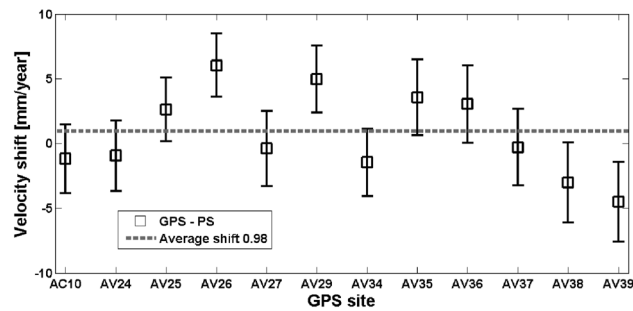
Figure 6. Shifts in velocity (mm/yr) computed from GPS and PSI with different spatial reference frames. The average shift is denoted by dashed line.

before 2009, which is also confirmed in the SBAS-derived deformation rate map in Figure 4b. Also, the GPS 3-D record indicates that AC10 moved toward the west and slightly to the south. Sites AV24 and AV25 demonstrate an overall linear trend with total deformation toward the satellite of approximately 20 mm from 2003 to 2010. For site AV27 the continuous linear deformation toward the satellite is more obvious, with a total deformation of about 40 mm over 7 years. The deformation records of sites AV 26 and AV 29 show less linear

behavior and offsets from GPS measurement, especially for period 2009 to 2010. The offset between the PSI and GPS displacements at site AV26 might be due to the localized atmosphere contamination that will be further discussed in section 4.2. The difference at AV29 is mainly due to lack of nearby PS points around GPS station, as the average distance between PS points to GPS site is about 887 m as listed in Table 3. Overall, the displacements at most points are upward and away from the volcano that both the GPS and PSI confirm the inflation of Westdahl since 2003, which is consistent with standard InSAR processing results [*Lu and Dzurisin*, 2014].

The comparison of sites around Shishaldin is shown in Figure 8, where an interesting phenomenon is captured by the PSI measurements. First of all, the time series of site AV38 demonstrates a negative trend before the middle of 2004, followed by a positive trend after that. The similar but less obvious trend can also be found for sites AV34 and AV35. This matches the time of the 2004 Shishaldin eruption from 17 February to 14 May [*Alaska Volcano Observatory*, *A*, 2009] as shown with dashed bars in Figure 8. However, these sites are located 15 to 30 km away from Shishaldin. The sites on Shishaldin Volcano, AV36, AV37, and AV39, show no change in displacement at that time. These sites would be expected to record a stronger volcanic deformation from a volcanic source underneath Shishaldin if that had caused the deformation at the other sites around the volcano. Thus, the cause of the observed deformation is not clear. The GPS deformation signals at AV37 and AV39 are rather similar, while the PSI measurements at AV39 are relatively noisy. Neither the GPS nor PSI provides any indication of a coeruptive signal. An earlier study showed that Shishaldin Volcano did not have significant coeruptive ground deformation during both its 1995–1996 and 1999 eruptions [*Moran et al.*, 2006]. That study covered the areas around the sites AV36, AV37, and AV39. Thus, the behavior we see in our study confirms that within the same area there is no obvious volcanic ground deformation.

4.2. Comparison With Different PSI Parameter Setting

We also compare the GPS measurements with PSI time series computed using different temporal filter settings to demonstrate the performance of the optimal temporal filter defined in section 3.1. The same procedure for reference frame difference compensation was applied to the results using filter length $\hat{T}$ of 70 days instead of 175 days. The statistics, residual mean (offset), and standard deviation (σ) at every GPS site, computed as the GPS minus PSI time series over the common time interval, are listed in the last two pairs of columns of Table 3. From the residual offset in Table 3 at site AV26, it is notable that the bias has already existed for 70 days window. Thus, rather than the underestimation from optimal window setting, the offset we see in Figure 7d could be mainly explained by localized artifacts (e.g., atmospheric distortions) that were not well compensated in the temporal filter approach due to acquisition gaps in 2007 to 2010.

As listed in the last column of Table 3, the optimized window provides about equal or smaller residual standard deviations at 10 out of 13 GPS sites. The average improvement is less than 1 mm per site. This suggests that the window length has only a small effect on the results at the evaluated GPS site locations. A better example that demonstrates the benefit brought by the optimal filtering setting is shown in Figure 8g, in which the PSI time series is produced by using a 70 day window setting. Comparing to Figure 8a, we can see that two different linear trends in 2004 and 2005 were introduced in Figure 8g that are likely to be artificial features caused by an unsuccessful reduction of atmospheric delays with the filter having short
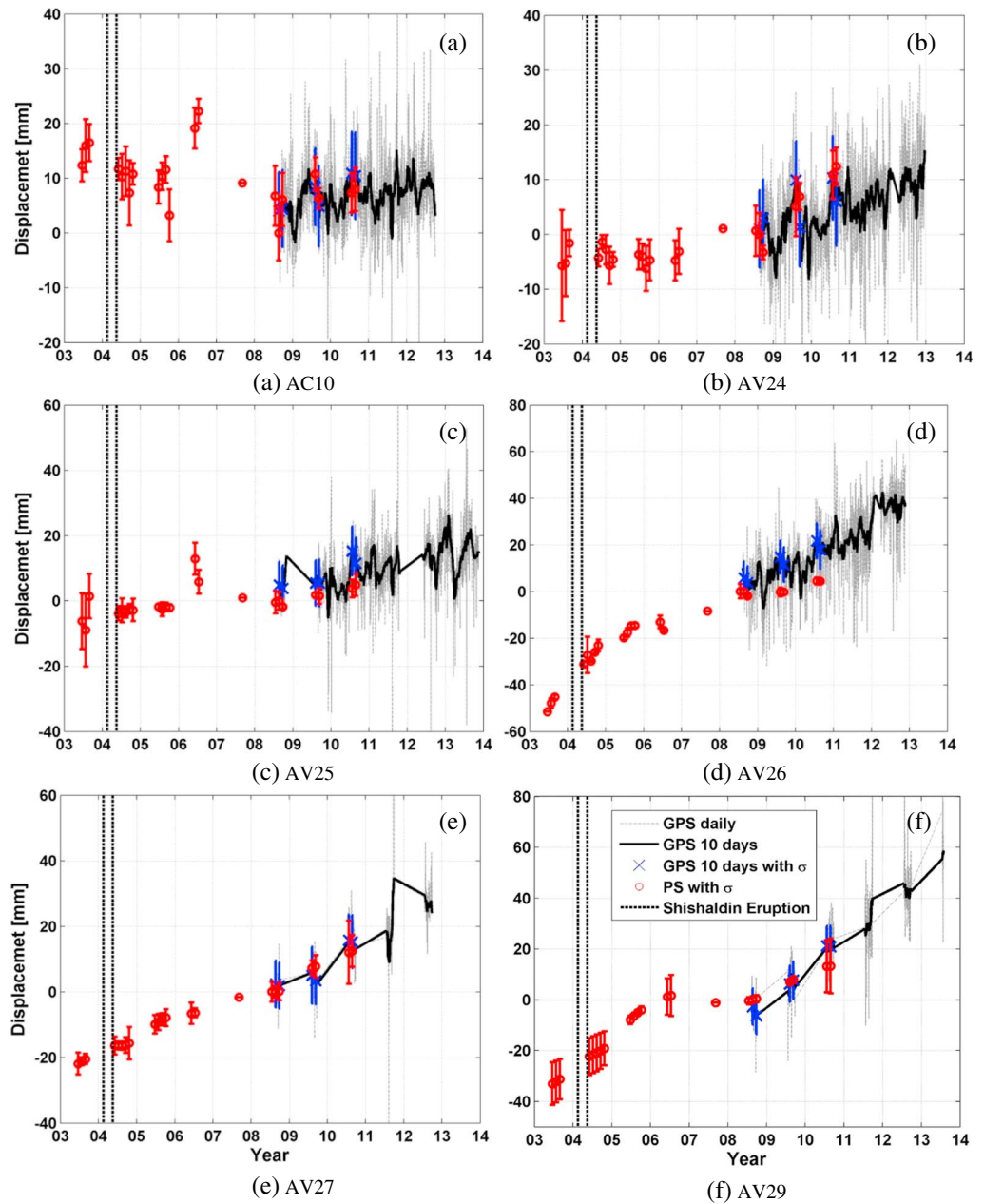
Figure 7. Comparison of GPS and PSI LOS time series measurements around Westdahl; *x* axes date format is yy; the eruption period in 2004 at Shishaldin is marked with dashed bars; red markers denote the PSI measurement with error bounds (σ); grey lines denotes GPS daily measurements; black line denotes 10 days averaged GPS measurements; and blue markers are the highlights of GPS 10 days average at corresponding SAR acquisition time with error bounds (the same for Figure 8).

window length (70 days). This indicates that the optimal filter approach is able to better balance the noise reduction and the deformation signal recovery.

5. Source Model Inversion for Westdahl Volcano and Fisher Caldera

5.1. Westdahl Volcano

In this section, we apply a volcano source model inversion to the PSI-derived motion time series of Westdahl Volcano. According to the study of *Mann and Freymueller* [2003], there is no significant strain accumulation
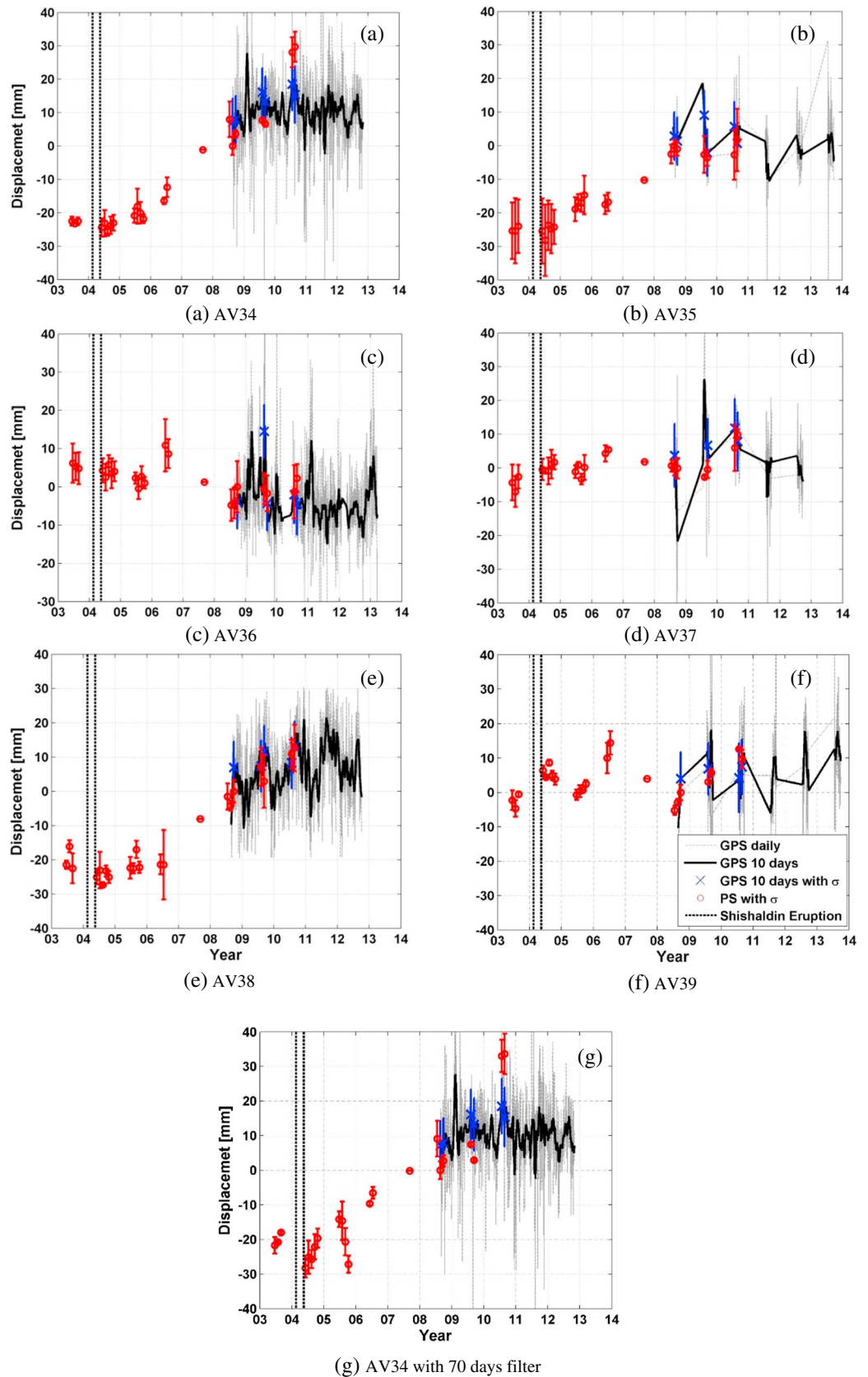
Figure 8. Comparison of GPS and PSI LOS time series measurements close to Shishaldin.

due to the locked subduction zone across the entire island, so the contribution from nonvolcanic sources over the Westdahl region is assumed to be small. Hence, without compensating deformation from any other source, the one-way displacement time series derived from PSI are used as input for estimation of a volcano source model. A Mogi source inversion [*Mogi*, 1958] was applied to the study of Westdahl Volcano as suggested by previous studies [*Mann and Freymueller*, 2003; *Lu et al.*, 2003, 2000; *Lu and Dzurisin*, 2014]. A rectangular region around Westdahl Volcano was selected, and the northeastern part of Westdahl close to Fisher Caldera was masked out to reduce the effect of displacement signals from Fisher on the Westdahl source.

There are six unknown parameters to be estimated, the four source model parameters (north, east, depth, and volume change ΔV) and two phase ramp parameters (north-south slope and east-west slope). The ramp parameters are supposed to be small, since the orbit residuals should have been already minimize in PSI processing. The PSI displacement time series without compensating the spatial reference difference between PSI and GPS measurement are used for the inversion, which have the average displacement field being zero within the cropped area. The spatial average of the model is subtracted from the model predictions during the inversion process. Given that there is only limited strain accumulation due to the locked subduction zone in this region [*Mann and Freymueller*, 2003], the spatial reference frame of Mogi model numerical simulations and PSI measurements is assumed to be the same.

As shown in Figure 3, the differences between the computed cumulative displacements at different months within the same year are very small. The yearly increment inflation signal is not used for the inversion study due to the subtle deformation signal and low signal-to-noise ratio. Instead, we have averaged the displacement results to obtain the annual averages.

The spatial distribution of coherent points in the PSI significantly impacts the source model inversion. As shown in Figure 4a, the point density around Westdahl is not evenly distributed; the south side of Westdahl peak shows fewer points than the north side. Moreover, the area close to Westdahl peak has no data due to loss of coherence so that the region most affected by the volcanic deformation has no coverage, which destabilizes the inversion. Thus, two sets of inversions are applied to the PSI displacement time series to determine the average horizontal location, average source depth, and volume change time series. The first inversion uses the average PSI data to determine the average horizontal location and average source depth of a Mogi source, and the second inversion estimates the time history of the volcano source volume change using the fixed source location derived from the first inversion.

In the first inversion, GPS velocities for the period 2008 to 2010 are compared to the PSI measurements to further compensate the slope ramp residuals in the PSI velocity map, given that the GPS measurements are not affected by these slope ramp errors. Thus, in the first inversion the slope ramp parameters are not estimated. The volcanic source model parameters are given relaxed bounds that extend beyond the detected source centers in previous studies [*Lu et al.*, 2003; *Mann and Freymueller*, 2003]. The estimated source location is 6.9 ± 0.9 km below sea level (bsl) and about 3.6 km north-northwest of Westdahl peak [*Alaska Volcano Observatory*, *A*, 2009] toward 350° azimuth from north (54. 55° ± 0.25 km north, 164.66° ± 0.2 km west, red markers in Figure 9). Figure 9 demonstrates the modeled ground deformation rate, which is the sum of the simulations generated separately by the corresponding best fit analytical source models of Westdahl Volcano and Fisher Caldera (see section 5.2). The solution for Westdahl is approximately 2 km northwest of the previous GPS study-suggested volcano source position for the period 1998 to 2001 [*Mann and Freymueller*, 2003] (black plus sign in Figure 9). The best fit location is close to the northwest end of the uncertainty range of the GPS-suggested Mogi source center. The average source depth is consistent with source depth ($7.2^{+2.3}_{-1.2}$ km) from the same GPS study. Thus, the source location at Westdahl appears to be close to the result in earlier period. The estimated average volume change rate for period 2003 to 2010 is $2.4 \pm 0.2 \times 10^{6}\,\mathrm{m}^{3}$/yr, which is about one third of the GPS result for 1998 to 2001 ($6.7^{+3.3}_{-1.8} \times 10^{6}\,\mathrm{m}^{3}$/yr).

Based on the result from the first inversion, the second inversion is carried out by fixing the average horizontal locations and source depth and computing the ΔV and the two ramp parameters from the yearly cumulative displacement time series. In this case, the modeled ramp rates from GPS measurement in the first inversion are removed from the cumulative displacement maps. However, in case there are scattered ramp residuals in every displacement map, the NS and EW ramp coefficients will be estimated. We compare GPS cumulative displacement measurements to PSI measurements, for periods of 2008 to 2009 and 2008 to 2010, and model the scattered slope ramp residual in the corresponding time intervals. This provides the slope ramp bound in the

GONG ET AL.
1187
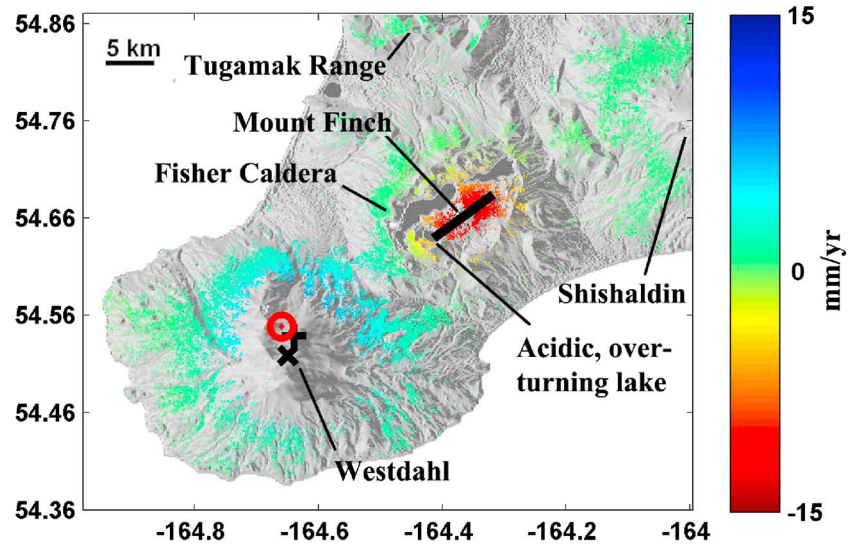
Figure 9. Demonstration of total displacement rate that is the summation of modeled deformation by the best fit point source for Westdahl Volcano and sill source for Fisher Caldera. The red markers are the best fit point source location and bold bar is the sill location. The cross denotes the Westdahl peak [*Alaska Volcano Observatory*, 2014] and the suggested volcano source location from previous InSAR study [*Lu et al.*, 2003]; the plus sign denotes the source location from previous GPS study [*Mann and Freymueller*, 2003].

compensated PSI cumulative displacement maps, ±0.5 mm/km. The estimates of ΔV time series and the ramp coefficients are listed in Table 4. The results change only a little if we assume that the ramp parameters are zero.

The inverted rate of ΔV decreases with time. *Lu et al.* [2003] proposed that cumulative ΔV is an exponential decaying function of time. With all the cumulative ΔV estimates referenced to the first SAR acquisition time on 25 July 2003, their model can be written as equation (4).

$$\Delta V_j = \left(1 - e^{-k \cdot t_j}\right) \cdot Q_0 \cdot k / \beta \tag{4}$$

where t is the time interval between 25 July 2003 and the rest of acquisitions, β is the constant defined in Mogi source model [*Mogi*, 1958], Q_0 is the initial magma flux into the reservoir, and k is a physical parameter that describes the frictional loss factor, magma viscosity, steady state change in magma reservoir volume, and length as well as the radius of the conduit (1/k is the so-called time constant) [*Dvorak and Okamura*, 1987; *Lu et al.*, 2003]. Similar to previous studies, k is treated as a single parameter and estimated with Q_0 by searching through the parameter space of k. The best fitting solution for equation (4) is found at $k = 0.15$ and $Q_0 = 54.2 \times 10^6\,m^3/yr$, which has an R^2 of 0.93. In addition to the exponential model, we also applied a weighted linear regression to our data in order to model temporal change of ΔV that results an R^2 of 0.89, which is lower than the R^2 for the exponential decaying model. Thus, the cumulative ΔV time series are better explained by the exponential decaying model than the linear model. In Figure 10, the corresponding cumulative ΔV time series estimated from Mogi source inversion are denoted by gray dot with their error bounds denoted by gray bars. The error bars show the 95% confidence level of the volume change

Table 4. Time Series of Volcano Source Volume Change and Corresponding Slope Ramp Estimates With Fixed Source Locations[a]

	2004	2005	2006	2007	2008	2009	2010
ΔVolume ($10^6\,m^3$)	5.15	11.73	11.84	15.04	16.34	19.22	24.24
ΔVolume sd. ($10^6\,m^3$)	0.36	0.16	0.55	0.96	1.53	2.34	0.53
EW ramp (mm/km)	0.27	−0.03	−0.24	0.04	0.48	0.07	−0.48
EW ramp σ (mm/km)	0.02	0.01	0.03	0.05	0.07	0.11	0.03
NS ramp (mm/km)	0.22	−0.12	−0.25	−0.09	−0.05	−0.14	−0.30
NS ramp σ (mm/km)	0.03	0.01	0.04	0.07	0.11	0.17	0.04

[a]σ denotes standard deviation; ΔVolume denotes volume change.
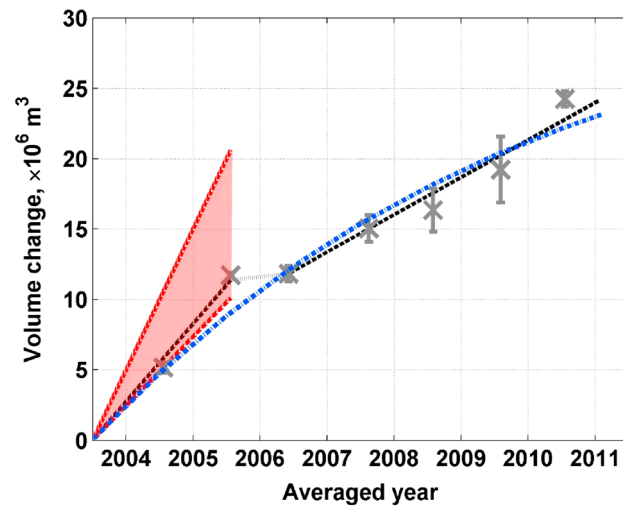
Figure 10. Estimated volume changes from point source modeling of PSI deformation measurements. The blue dash-dotted line denotes modeled cumulative volume change with exponential decaying function. The dashed line with black color and dotted line with gray color denote the modeled result with step linear function. The shaded zone represents the suggested volume change with upper and lower bounds from the GPS study for 1998 to 2001 [*Mann and Freymueller*, 2003].

measurements, which are calculated from the residuals of each inversion. The modeled cumulative ΔV with the exponential decaying function is denoted by the blue dash-dotted line in Figure 10.

We also apply the exponential decaying model with the same temporal reference used in the study by *Lu et al.* [2003] and their model parameter estimates ($k = 0.17$ and $9.2 \times 10^6\,m^3/yr$) to fit our time series measurements. However, the R^2 indicates a poor fit. We conclude that previously determined exponential decaying model parameters are not sufficient to explain the volume change of Westdahl over the full time span since the 1991 eruption.

Lu and Dzurisin [2014] suggest that the volume change rate of Westdahl Volcano through the 2003 to 2010 period is not fully consistent. The PSI-derived cumulative ΔV time series in Figure 10 also suggests that there might be two stages of volume change with a pause in 2005 to 2006, where the refilling of the magma source nearly stopped before restarting in the year after. This episodic pulse phenomenon observed for period 2005 to 2006 resembles studies in the other volcanoes, e.g., what was observed at Okmok volcano, where three distinct inflation episodic pulses could be identified [*Fournier et al.*, 2009]; at Kīlauea Volcano during 2003 to 2007, where the transient increase in magma supply was observed [*Poland et al.*, 2006]; and at Cordón Caulle volcano for 2011 to 2012, where multiple pulses of uplift in volcanic deformation have been found [*Jay et al.*, 2014]. We speculate that the volcanic inflation at Westdahl is also pulsed, rather than decaying steadily. Thus, we evaluate the linear rate of volume change in two time periods (2003 to 2005 and 2006 to 2010). The demonstration of linear rates for these two different stages (demonstrated by black dashed lines) and presumed pause (gray dotted line) is shown in Figure 10. The estimated volume change rate of the first stage (2003 to 2005) is $5.5 \times 10^6\,m^3/yr$, of the second stage (2006 to 2009) is $2.7 \times 10^6\,m^3/yr$, and the gradients between first and second stages (2005 to 2006) is $0.11 \times 10^6\,m^3$. Note that the linear rate of the first stage is within the error bounds of the average volume change rate estimated from the previous GPS study for the period 1998 to 2001 ($6.7^{+3.3}_{-1.8} \times 10^6\,m^3/yr$) [*Mann and Freymueller*, 2003], which is shown in Figure 10 by the red area and dashed red lines denoting the upper and lower bounds of the rate. This suggests that the Westdahl volume changes for periods from 1998 to 2001 and 2003 to 2005 belong to the same stage, and that this stage might be followed by a pause from 2005 to 2006 and a slower volume change rate after 2006. It seems that the measurement for 2010 is an outlier to this step linear model, as its volume change and error bounds estimates lie above the model prediction. Future observations are needed to determine whether the 2010 result is merely an outlier to the model or if it marks the beginning of a new stage in the magma system.

5.2. Fisher Caldera

To understand the long-term subsidence of Fisher Caldera, we have also applied the volcano source model inversion to the PSI-derived average deformation rate map over Fisher and determined its analytical source parameters. A polygon area around Fisher Caldera has been drawn to minimize the contribution from the other deformation sources. We have applied inversions with sill model [*Okada*, 1985], spheroid model [*Yang et al.*, 1988], and Mogi model [*Mogi*, 1958] based on experiences from other geodetic studies [*Mann and Freymueller*, 2003; *Lu and Dzurisin*, 2014] and spatial features of deformation observed in this study. The same inversion strategy that was used to discover the average source location of Westdahl Volcano has been applied to study Fisher Caldera.

By comparing misfits from different source model inversions and applying *F* tests, it shows that the sill model fits the observed deformation field best. The inversion result suggests that the sill source was approximately underneath the Fisher Caldera center. The source center (54. 66° ± 0.8 km north, 164.37° ± 1.1 km west) is near Mount Finch (Figure 9), which was the suggested vent for the 1826 eruption [*Stelling et al.*, 2005]. It is also the region showing maximum deformation during 2003 to 2010 in presented study and in earlier period in 1990s [*Lu and Dzurisin*, 2014]. The sill plane has a depth of 5.5 ± 0.1 km bsl and is 7.9 ± 0.1 km in length, 0.54 ± 0.3 km in width, and strikes in N52° ± 0.6°E. The amount of the contraction is 0.33 + 0.4/−0.1 m/yr.

The sill model identified in this study is consistent with the suggestion from *Lu and Dzurisin* [2014] for period 1993 to 2000. For comparison, in an additional test, we also allowed the sill plane dipping in different direction to fit the observed deformation field in Fisher Caldera. The result suggests that the best fit rectangular plane has the same location as well as strike direction and dips to southwest direction at 10°. However, the *F* test indicates that the rectangular dislocation source with 10° dipping angle does not fit the observation better than the horizontal sill. Both the best fit Mogi and spheroid model suggest the consistent center location that is around Mount Finch. The Mogi source has a similar depth at about 5.6 km bsl. The best fit spheroid model suggests a shallower source at about 3.5 km bsl with the major axis of about 6.7 km and semiaxis of about 0.9 km. The best fit parameters of Mogi source and spheroid source also agree with the model inversion results from *Lu and Dzurisin* [2014] for the period of 1993 to 2000. Thus, the study on the analytical source model suggests that the trigger of subsidence observed at Fisher Caldera is stable and consistent during periods from 1993 to 2000 and 2003 to 2010. For studied time span (2003 to 2010), it can be better analytically modeled as the sill source.

Taking into account the study result presented above and those from the other geodetic studies of Fisher Caldera [*Mann and Freymueller*, 2003; *Lu and Dzurisin*, 2014], it shows no evidence of uplift and approximately steady subsidence that is likely triggered by the same stable source since at least the 1990s to 2010. Other than ground deformation, hydrothermal activities at Fisher Caldera have been recorded [*Stelling et al.*, 2005], including hot spring, fumaroles, and temporary plume in 2000. For instance, there is an acidic overturning lake located southwest of the caldera [*Mann and Freymueller*, 2003; *Stelling et al.*, 2005] (shown in Figure 9) that is overlying with the southwest end of determined sill source.

6. Geophysical Interpretation

Based on the deformation time series maps extracted and analyzed above, the deformation observations from 2003 to 2010 over the three active volcanoes on Unimak can be summarized as follows.

6.1. Westdahl Volcano

Although Westdahl Volcano is still inflating, its average LOS velocity over coherent areas is now less than 1 cm/yr. This is much smaller than the rate of 2 cm/yr that was observed in 1998 to 2001 time span. The point source model inversion indicates an inflation source center at about 3.6 km north-northwest of Westdahl peak [*Alaska Volcano Observatory*, A, 2009] (toward 350° azimuth from the north) with depth of 6.9 ± 0.9 km bsl. The depth agrees with the previous GPS study from 1998 to 2001 [*Mann and Freymueller*, 2003]. There are some inconsistencies of the source horizontal location among the presented study and those from the GPS [*Mann and Freymueller*, 2003] and InSAR [*Lu et al.*, 2003] studies for earlier period. Both this study and previous GPS result suggest that the source center is located about north of Westdahl peak that is also the source center determined by the previous InSAR study. It is recommended to study additional geological or geophysical data to confirm and understand stability of the source horizontal location. The volume change time series shows a clear slowing down of inflation at Westdahl since 1998. Although the previously determined exponential decaying parameters by *Lu et al.* [2003] do not fit our observations, the proposed exponential decaying function is able to well approximate the magma refilling time series of Westdahl for the period 2003 to 2010. Our result also suggests that the slowing down of magma volume change rate at Westdahl could be related to a pause in 2005 to 2006, when there is little magma added into the volcano system. Based on measurements from this study and the previous ones at Westdahl Volcano [*Mann and Freymueller*, 2003; *Lu et al.*, 2003; *Lu and Dzurisin*, 2014], and also the episodic pulse phenomenons observed in geophysical studies of other volcanic systems, we can consider a scenario of episodic magma refilling between any two eruptions of Westdahl. After an eruption stops, the volcano source begins to refill in pulses, producing several longer-term exponentially decaying processes. For future study at Westdahl Volcano, we

recommend further geodetic monitoring with data acquired with higher sampling rate (e.g., new satellite data with shorter revisiting time or GPS observation) to confirm the episodic magma intrusion.

6.2. Fisher Volcano

The deformation field over Fisher Caldera is more consistent and linear with time, and subsidence has continued with a maximum LOS velocity of about 16 mm/yr. This result has been confirmed through both PSI and SBAS techniques, both of which show good agreement with the historical GPS result from 1998 to 2001 [*Mann and Freymueller*, 2003] and the InSAR result from 1993 to 2000 [*Lu and Dzurisin*, 2014]. Moreover, the parameters of a best fit analytical model (sill source) derived from presented study are consistent with *Lu and Dzurisin* [2014] for the period 1993 to 2000. We therefore conclude that the source underneath the Fisher Caldera is stable that causes the subsidence for about two decades since 1990s.

Long-term subsidence of this nature has been previously reported in a number of volcanic systems, including Yellowstone Caldera [*Dzurisin et al.*, 1990; *Wicks et al.*, 2006], Medicine Lake Volcano [*Parker et al.*, 2014; *Poland et al.*, 2006], Campi Flegrei [*Todesco et al.*, 2014], and Aniakchak and Mount Kupreanof volcanoes in the Aleutian Islands [*Lu and Dzurisin*, 2014]. The reported subsidence rates at these locations range from a few millimeters to tens of centimeters per year. Conceptual mechanisms of the long-term subsidence include the volume or pressure changes of the magma sources, pressure reduction of the hydrothermal systems, or both [*Fournier*, 1999; *Lu and Dzurisin*, 2014; *Mann and Freymueller*, 2003; *Todesco et al.*, 2014].

At Fisher Caldera, the subsidence may be caused by the thermal contraction and degassing of the underlying crystallizing magma body, which could either be an active magma reservoir [*Lu and Dzurisin*, 2014] or a pre-1992 intrusive sill. The vigorous hydrothermal activities in the caldera floor, e.g., the acidic lake [*Stelling et al.*, 2005], also provide evidences for the release of volatiles. Using the sill depth (about 5.5 km bsl) and contraction rate (0.33 m/yr) determined in this study, and assuming a steady volume change rate across two decades, we have calculated the required original sill thickness by following the one-dimension thermal contraction model used in *Mann and Freymueller* [2003] for basalt to intermediate andesite (corresponding to the magma composition at Fisher Caldera [*Stelling et al.*, 2005]). Our result shows that the required thickness of the sill body is 100 m to 200 m, if assuming contraction alone; however, if a partial volume change is attributed to loss of volatiles (assuming water only for simplicity) released during crystallization, the required magma thickness can be about 50 m by assuming 30% of the total water content has degassed and lost. The total water content in this context denotes the water mass fraction of the water saturated magma at the defined source depth, pressure, and magma type, e.g., in this study for Fisher Caldera the water fraction is 4 wt % to 4.5 wt % [*Newman and Lowenstern*, 2002]. Thus, with the simple thermal contraction model, it requires a giant magma body to support the long-term subsidence. However, source depth and its surrounding geophysical condition must be considered in proposing the cooling and crystallization process [*Parker et al.*, 2014]. If, for instance, a magma reservoir overlies an intrusive complex, the resulting geothermal conditions could complicate the cooling and contraction process. In this scenario, it may not be sufficient to use the simple thermal contraction and degassing model to account for volume change. Further geological surveys would be helpful to analyze the geophysical condition underneath Fisher Calder and to support researchers in exploring the cause of the observed subsidence. We therefore hypothesize that magma cooling and crystallization is still a possible explanation of the observed deformation.

The depressurization of an underlying hydrothermal system is also likely a cause driven the observed subsidence [*Lu and Dzurisin*, 2014; *Mann and Freymueller*, 2003]. In such scenario, the uplift (pressurization) and subsidence (depressurization) would occur as episodes, which have been observed in studies of other calderas [*Fournier*, 1999; *Todesco et al.*, 2014; *Wicks et al.*, 2006]. Pressurization results from the interaction between magma and the hydrothermal system, sealed by a brittle-plastic transition layer [*Fournier*, 1999]. Depressurization could be due to the fading of magma feeding and/or permeability-related degassing [*Fournier*, 1999]. In the latter case, the rupture of the brittle-plastic layer would allow the pressure reduction and could be indicated by an earthquake swam, such as that occurring at Yellowstone Caldera in 1985 [*Waite and Smith*, 2002]. The subsidence in Fisher Calder, however, has been steady since the 1990s, which suggests that either the observed subsidence is part of the uplift-subsidence cycle or the hydrothermal system is not the cause of the observed subsidence. Additionally, since the installation of seismic networks on Unimak

Island in 1998, there has been no evidence of earthquake swarms related to Fisher Caldera [*Lu and Dzurisin*, 2014]. Thus, longer-term monitoring is necessary to understand the role of the hydrothermal system as a potential mechanism of the ground subsidence at Fisher Caldera.

Overall, while thermal contraction of crystallizing magma and/or the hydrothermal cycle are both likely contributors; further data provided by geodetic and geological studies are needed in order to distinguish between each mechanism. Thus, a longer-term monitoring and surveying effort is suggested to identify the primary mechanism of the long-term subsidence at Fisher Caldera.

6.3. Shishaldin Volcano

Shishaldin Volcano has a more active eruption record compared to the other two volcanoes discussed above but with a puzzling lack of observable deformation. A previous attempt to use InSAR techniques at Shishaldin Volcano was not able to detect significant deformation during the two eruptions in 1995 and 1999 [*Moran et al.*, 2006]. We find that the same was true for the 2004 eruption at the Shishaldin cone, which suggests either a deep volcanic source (more than 10 km) or a fast refilling system and/or a shallow magma source [*Lu and Dzurisin*, 2014; *Moran et al.*, 2006]. However, the regions east of Shishaldin (approximately 15 km away) and north of Fisher Caldera (the Tugamak range, approximately 30 km away) contain some deformation signals, which have also been confirmed by GPS measurements after 2008 [*UNAVCO*, 2013]. Moreover, the presented InSAR study for 2003 to 2010 shows that the deformation is temporally correlated with Shishaldin eruption in 2004. Despite this correlation, the summation of ground deformation rates calculated from the best-fit volcanic source models of Westdahl Volcano and Fisher Caldera (see Figure 9) dose not fit well with the observed deformation at Tugamak range and around Shishaldin Volcano (see Figures 3 and 4). We suspect that there are other deformation sources in the Unimak Island that have not yet been identified. At the current time, we do not have enough information to conclude whether these signals are due to a deep volcanic pressure source underneath Shishaldin, nor do we have enough information to explain the absence of deformation around Shishaldin peak.

7. Summary and Conclusions

We present a study using satellite radar interferometry methods for long-term volcano monitoring at Unimak Island, Alaska. Numerical weather prediction model forecasting products are used to assist the time series InSAR technique to optimally mitigate atmospheric artifacts. Several comparisons among InSAR deformation measurements derived from different processing techniques (PSI and SBAS) or processing controls (various settings on temporal smoothing) and GPS geodetic records have been done for the quality assessment and geophysical interpretation. These include the evaluation of the PSI-reconstructed velocity map to SBAS-processed results, comparisons of PSI-derived deformation time series to both historical and current GPS time series measurements, and the assessment of deformation series extracted from different PSI temporal filter settings. The results demonstrate that this InSAR method is able to mitigate atmospheric signals with high quality and improve the confidence of the reconstructed deformation time series.

The PSI-derived deformation fields are used for geophysical interpretation for three active volcanoes, namely, Westdahl Volcano, Fisher Caldera, and Shishaldin Volcano. The conclusions listed below can be made from our quantitative study.

1. Westdahl Volcano is still inflating but at a lower rate than in the period before 2001. Its magma source can be described by a Mogi model, whose location is approximately 6.9 km bsl and 3.6 km north-northwest of Westdahl peak and its volume change rate decrease with time. The exponentially decaying volume change model proposed by *Lu et al.* [2003] can be used to explain the volume change derived from this study for 2003 to 2010, although the previously defined model parameters for period 1992 to 2000 are insufficient to model our observations. Using the exponential decaying model [*Lu et al.*, 2003] to explain the temporal evolution of volume change of Westdahl Volcano remains viable. We suggest the reestimation of the exponential decaying parameters for full time span since its last eruption in 1991 to better reveal the overall volume change dynamic in the eruption cycle. We also favor to speculate that the magma refilling between two eruptions of Westdahl consists of multiple episodic pulses, which would produce long-term exponentially decaying processes. It can be further confirmed by future long-term geological study and geodetic monitoring.

2. Fisher Caldera has been subsiding with a steady linear rate since 1990s. Geodetic measurements and the source model inversion suggest that the subsidence source remains stable for about two decades. The bets fit analytical sill source model is centered at Mount Finch at depth of about 5.5 km bsl. It could result from the magma contraction and crystallization and degassing, and/or depressurization of the hydrothermal system. With current geological and geophysical studies, it is difficult to distinguish the primary trigger. We recommend the future geophysical monitoring and surveying to better understand the driven mechanism of subsidence at Fisher Caldera.

3. Shishaldin Volcano shows no observable deformation signals near its peak. However, deformation changes in time correlated with its 2004 eruption are observed more than 30 km away from Shishaldin peak on the Tugamak range and approximately 15 km toward the east of Shishaldin. However, the source of those movements is not clear. Further geodetic studies and seismic monitoring at Shishaldin and these regions are suggested.

References

Agram, S. P., F. Casu, H. A. Zebker, and R. Lanari (2011), Comparison of persistent scatterers and small baseline time-series InSAR results: A case study of the San Francisco Bay area, *Geosci. Rem. Sens. Lett. IEEE*, *8*(4), 592–596.

Alaska Volcano Observatory, A. (2009), Database of Alaska Volcano Information. [Available at http://www.avo.alaska.edu/.]

Buurman, H. (2013), Volcano Seismicity in Alaska, PhD dissertation, 163 pp., Dep. of Geol. and Geophys., Univ. of Alaska, Fairbanks.

Cimini, D., N. Pierdicca, E. Pichelli, R. Ferretti, V. Mattioli, S. Bonafoni, M. Montopoli, and D. Perissin (2012), On the accuracy of integrated water vapor observations and the potential for mitigating electromagnetic path delay error in InSAR, *Atmos. Meas. Tech.*, *5*, 1015–1030.

Dvorak, J. J., and D. Dzurisin (1997), Volcano geodesy: The search for magma reservoirs and the formation of eruptive vents, *Rev. Geophys.*, *35*(3), 343–384.

Dvorak, J. J., and A. T. Okamura (1987), A hydraulic model to explain variations in summit tilt rate at Kilauea and Mauna Loa volcanoes, in *Volcanism in Hawaii*, edited by T. L. Wright et al., U.S. Geol. Surv., Washington.

Dzurisin, D. (2003), A comprehensive approach to monitoring volcano deformation as a window on the eruption cycle, *Rev. Geophys.*, *41*(2), 1001, doi:10.1029/2003RG000134.

Dzurisin, D., J. C. Savage, and R. O. Fournier (1990), Recent crustal subsidence at Yellowstone Caldera, Wyoming, *Bull. Volcanol.*, *52*(4), 247–270.

Ferretti, A., C. Prati, and F. Rocca (2000), Nonlinear subsidence rate estimation using permanent scatterers in differential SAR interferometry, *IEEE Trans. Geosci. Remote Sens.*, *38*(5), 2202–2212.

Foster, J., J. Kealy, T. Cherubini, S. Businger, Z. Lu, and M. Murphy (2013), The utility of atmospheric analyses for the mitigation of artifacts in InSAR, *J. Geophys. Res. Solid Earth*, *118*, 748–758, doi:10.1002/jgrb.50093.

Fournier, R. O. (1999), Hydrothermal processes related to movement of fluid from plastic into brittle rock in the magmatic-epithermal environment, *Econ. Geol. Bull. Soc.*, *94*(8), 1193–1211.

Fournier, T., J. Freymueller, and P. Cervelli (2009), Tracking magma volume recovery at Okmok volcano using GPS and an unscented Kalman filter, *J. Geophys. Res.*, *114*, B02405, doi:10.1029/2008JB005837.

Freymueller, J., and J. Beavan (1999), Absence of strain accumulation in the western Shumagin segment of the Alaska subduction zone, *Geophys. Res. Lett.*, *26*(21), 3233–3236.

Gong, W., and F. Meyer (2012), Optimized filter design for irregular acquired data stack in persistent scatterers synthetic aperture radar interferometry, 2012 IEEE International Geoscience and Remote Sensing Symposium Munich, Germany, 22–27 July 2012.

Gong, W., F. J. Meyer, and S. Liu (2011), Numerical weather model assisted time series InSAR processing for geophysical application, 2011 ESA Fringe Workshop, European Space Agency, Frascati, Italy, 19–23 September.

Gong, W., F. J. Meyer, P. Webley, and D. Morton (2013), Performance of the high-resolution atmospheric model HRRR-AK for correcting geodetic observations from spaceborne radars, *J. Geophys. Res. Atmos.*, *118*, 11,611–11,624, doi:10.1002/2013JD020170.

Hanssen, R. (2001), *Radar Interferometry: Data Interpretation and Error Analysis*, Kluwer Acad., Netherlands.

Hooper, A., D. Bekaert, K. Spaans, and M. Arıkan (2012), Recent advances in SAR interferometry time series analysis for measuring crustal deformation, *Tectonophysics, 514–517*, 1–13.

Jay, J., F. Costa, M. Pritchard, L. Lara, B. Singer, and J. Herrin (2014), Locating magma reservoirs using InSAR and petrology before and during the 2011–2012 Cordón Caulle silicic eruption, *Earth Planet Sci. Lett.*, *395*(0), 254–266.

Lee, C. W., Z. Lu, H. S. Jung, J. S. Won, and D. Dzurisin (2010), Surface deformation of Augustine Volcano, 1992–2005, from multiple-interferogram processing using a refined small baseline subset (SBAS) interferometric synthetic aperture radar (InSAR) approach, in The 2006 Eruption of Augustine Volcano, Alaska, edited by J. A. Power et al., *U.S. Geol. Surv. Prof. Pap.*, *1769*, 453–465. [Available at http://pubs.usgs.gov/pp/1769/chapters/p1769_chapter17.pdf.]

Liu, S. (2012), Satellite radar interferometry: Estimation of atmospheric delay, 203 pp., PhD thesis, Delft Univ. of Technology.

Lu, Z. (2007), InSAR imaging of volcanic deformation over cloud-prone areas—Aleutian Islands, *Photogramm. Eng. Remote Sens.*, *73*, 245–257.

Lu, Z., and D. Dzurisin (2014), *InSAR Imaging of Aleutian Volcanoes: Monitoring a Volcanic Arc From Space*, Springer, Heidelberg, New York, doi:10.1007/978-3-642-00348-6.

Lu, Z., and J. T. Freymueller (1998), Synthetic aperture radar interferometry coherence analysis over Katmai volcano group, Alaska, *J. Geophys. Res.*, *103*(B12), 29,887–29,894.

Lu, Z., C. Wicks, D. Dzurisin, W. Thatcher, J. T. Freymueller, S. R. McNutt, and D. Mann (2000), Aseismic inflation of Westdahl Volcano, Alaska, revealed by satellite radar interferometry, *Geophys. Res. Lett.*, *27*(11), 1567–1570.

Lu, Z., T. Masterlark, D. Dzurisin, R. Rykhus, and C. Wicks Jr. (2003), Magma supply dynamics at Westdahl volcano, Alaska, modeled from satellite radar interferometry, *J. Geophys. Res.*, *108*(B7), 2354, doi:10.1029/2002JB002311.

Lu, Z., D. Dzurisin, C. Wicks Jr., J. Power, O. Kwoun, and R. Rykhus (2007), Diverse deformation patterns of Aleutian volcanoes from satellite interferometric synthetic aperture radar (InSAR), in *Volcanism and Subduction: The Kamchatka Region*, edited by J. Eichelberger et al., pp. 249–261, AGU, Washington, D. C.

Mann, D., and J. Freymueller (2003), Volcanic and tectonic deformation on Unimak Island in the Aleutian Arc, Alaska, *J. Geophys. Res.*, *108*(B2), 2108, doi:10.1029/2002JB001925.

Mogi, K. (1958), Relations between the eruptions of various volcanoes and the deformations of the ground surfaces around them, *Bull. Earthquake Res. Inst., Univ. Tokyo*, *36*, 99–134.

Moran, S. C., O. Kwoun, T. Masterlark, and Z. Lu (2006), On the absence of InSAR-detected volcano deformation spanning the 1995–1996 and 1999 eruptions of Shishaldin Volcano, Alaska, *J. Volcanol. Geotherm. Res.*, *150*, 119–131, doi:10.1016/j.jvolgeores.2005.07.013.

Newman, S., and J. B. Lowenstern (2002), VOLATILECALC: A silicate melt-H2O-CO2 solution model written in Visual Basic for excel, *Comput. Geosci.*, *28*(5), 597–604.

Okada, Y. (1985), Surface deformation due to shear and tensile faults in a half-space, *Bull. Seismol. Soc. Am.*, *75*(4), 1135–1154.

Parker, A. L., J. Biggs, and Z. Lu (2014), Investigating long-term subsidence at Medicine Lake Volcano, CA, using multitemporal InSAR, *Geophys. J. Int.*, *199*, 844–859, doi:10.1093/gji/ggu304.

Poland, M., R. Burgmann, D. Dzunisin, M. Lisowski, T. Masterlark, S. Owen, and J. Fink (2006), Constraints on the mechanism of long-term, steady subsidence at Medicine Lake volcano, northern California, from GPS, leveling, and InSAR, *J. Volcanol. Geotherm. Res.*, *150*, 55–78.

Schmidt, D. A., and R. Burgmann (2003), Time-dependent land uplift and subsidence in the Santa Clara valley, California, from a large interferometric synthetic aperture radar data set, *J. Geophys. Res.*, *108*(B9), 2416, doi:10.1029/2002JB002267.

Segall, P. (2010), *Earthquake and Volcano Deformation*, vol. xxiii, pp. 432–438, Princeton Univ. Press, Princeton, N. J.

Skamarock, W. C., J. B. Klemp, J. Dudhia, D. O. Gill, M. Barker, K. G. Duda, X. Y. Huang, W. Wang, and J. G. Powers (2008), A Description of the Advanced Research WRF Version 3, *NCAR Tech. Note NCAR/TN-475+STR*, doi:10.5065/D68S4MVH.

Stelling, P., J. E. Gardner, and J. Beget (2005), Eruptive history of Fisher Caldera, Alaska, USA, *J. Volcanol. Geotherm. Res.*, *139*, 163–183.

Todesco, M., A. Costa, A. Comastri, F. Colleoni, G. Spada, and F. Quareni (2014), Vertical ground displacement at Campi Flegrei (Italy) in the fifth century: Rapid subsidence driven by pore pressure drop, *Geophys. Res. Lett.*, *41*, 1471–1478, doi:10.1002/2013GL059083.

University Corporation for Atmospheric Research (2013), Database of NCEP FNL Operational Model Global Tropospheric Analyses, continuing from July 1999. [Available at http://rda.ucar.edu/datasets/ds083.2/.]

University NAVSTAR Consortium (2013), GNSS Data Archive Interface Version 2 (DAI v2). [Available at http://facility.unavco.org/data/.]

Waite, G. P., and R. B. Smith (2002), Seismic evidence for fluid migration accompanying subsidence of the Yellowstone caldera, *J. Geophys. Res.*, *107*(B9), 2177, doi:10.1029/2001JB000586.

Wicks, C. W., W. Thatcher, D. Dzurisin, and J. Svarc (2006), Uplift, thermal unrest and magma intrusion at Yellowstone caldera, *Nature*, *440*, 72–75.

Wood, C. A., and J. Kienle (1990), *Volcanoes of North America: United States and Canada*, 354 pp., Cambridge Univ. Press, Cambridge England, New York.

Yang, X. M., P. M. Davis, and J. H. Dieterich (1988), Deformation from inflation of a dipping finite prolate spheroid in an elastic half-space as a model for volcanic stressing, *J. Geophys. Res.*, *93*(B5), 4249–4257.